

The effect of hydration number on the interfacial transport of sodium ions

Jinbo Peng^{1,9,10}, Duanyun Cao^{1,10}, Zhili He^{2,10}, Jing Guo¹, Prokop Hapala³, Runze Ma¹, Bowei Cheng¹, Ji Chen⁴, Wen Jun Xie², Xin-Zheng Li^{5,6}, Pavel Jelínek^{3,7}, Li-Mei Xu^{1,6*}, Yi Qin Gao^{2*}, En-Ge Wang^{1,6,8*} & Ying Jiang^{1,6,8*}

Ion hydration and transport at interfaces are relevant to a wide range of applied fields and natural processes^{1–5}. Interfacial effects are particularly profound in confined geometries such as nanometre-sized channels^{6–8}, where the mechanisms of ion transport in bulk solutions may not apply^{9,10}. To correlate atomic structure with the transport properties of hydrated ions, both the interfacial inhomogeneity and the complex competing interactions among ions, water and surfaces require detailed molecular-level characterization. Here we constructed individual sodium ion (Na⁺) hydrates on a NaCl(001) surface by progressively attaching single water molecules (one to five) to the Na⁺ ion using a combined scanning tunnelling microscopy and noncontact atomic force microscopy system. We found that the Na⁺ ion hydrated with three water molecules diffuses orders of magnitude more quickly than other ion hydrates. *Ab initio* calculations revealed that such high ion mobility arises from the existence of a metastable state, in which the three water molecules around the Na⁺ ion can rotate collectively with a rather small energy barrier. This scenario would apply even at room temperature according to our classical molecular dynamics simulations. Our work suggests that anomalously high diffusion rates for specific hydration numbers of ions are generally determined by the degree of symmetry match between the hydrates and the surface lattice.

Determination of molecular-level details of hydration processes remains a great challenge, both experimentally and theoretically. Various spectroscopic techniques have been used to identify the structure and dynamics of solvated ions or molecules through vibrational fingerprints^{11–13}. However, all of these techniques suffer from poor spatial resolution and the difficulty of spectral assignment. Molecular simulations have also become powerful tools with which to investigate atomic-scale hydration properties^{2,14,15}, but the reliability of the results depends critically on many tunable factors¹⁴. Recently, scanning probe microscopy has provided an opportunity to probe interfacial water at the single-molecule or even submolecular level^{16–22}, but the application to ion hydration systems is not straightforward owing to the lack of controlled methods of preparing individual ion hydrates on the substrates and the high flexibility of their structures^{23,24}. Using an ultrahigh-resolution scanning tunnelling microscopy (STM) and qPlus²⁵ noncontact atomic force microscopy (AFM) combined system, here we studied the hydrated Na⁺ ion, an alkali metal ion abundant in natural water and biological solutions.

The Na⁺ hydrates (Na⁺·*n*D₂O, *n* = 1–5) were assembled in a controlled manner by progressively attaching single D₂O molecules to Na⁺ ions, which were extracted from the NaCl surface with a chlorine (Cl⁻)-terminated tip (for detailed procedures, see Methods and Supplementary Fig. 1). We found that the barrier for extracting the Na⁺ from NaCl was greatly suppressed with the assistance of water²⁶.

Figure 1a–e shows the atomic models, STM/AFM images (acquired with a CO tip²⁷) and AFM simulations of Na⁺·*n*D₂O clusters (*n* = 1–5). From the atomically resolved STM images, it can be clearly seen that Na⁺·D₂O, Na⁺·2D₂O, and Na⁺·3D₂O adsorb at the bridge sites, while Na⁺·4D₂O and Na⁺·5D₂O adsorb on top of the Cl⁻ sites. We found that the maximum number of water molecules in the first hydration shell is five (see Supplementary Fig. 2). Further addition of water to Na⁺·5D₂O results in formation of the second and higher hydration shells.

The AFM images of the ion hydrates were acquired within the weak-disturbance region where the high-order electrostatic force is dominant²¹, providing higher resolution and finer details than STM. The charge state of Na in the hydrates can be verified by comparing the AFM images and simulations (Supplementary Fig. 3). In the AFM images, the Na⁺ ion appears as a dark depression, mainly arising from the electrostatic attraction between the CO-tip apex and the Na⁺ ion. By contrast, the water molecule was imaged as a bright feature (white arrow in Fig. 1a) surrounded by a dark ring (white dashed curve in Fig. 1a), which are ascribed to the negatively charged O atom and the positively charged D atom, respectively²¹. The ‘standing’ water (that is, the molecular plane of the water molecule is perpendicular to the surface, in contrast to the flat-lying water molecules) of Na⁺·3D₂O (see the white arrow in Fig. 1c) shows a prominent protrusion caused by the Pauli repulsion force. The fuzzy feature in the AFM image of Na⁺·D₂O (see the blue arrow in Fig. 1a) may result from the flipping of water over Na⁺ in the presence of the tip (for more experimental evidence, see Supplementary Fig. 4). The AFM simulations based on a molecular mechanics model using a quadrupole tip (Methods) nicely reproduce all the experimental images. The comparison between the submolecular-resolution AFM image and simulation is important in determining the structure of ion hydrates (one example is shown in Supplementary Fig. 5).

Next we explored the transport of those hydrates. To activate their diffusion at low temperature (5 K), we used the inelastic electron tunnelling technique by injecting ‘hot’ (that is, with larger energy than those at the experimental temperature) electrons/holes into the Au substrate, which transport along the surface and transfer their energy to the hydrates^{28,29} (Fig. 2a). Figure 2b plots the diffusion probability of Na⁺·3D₂O and Na⁺·3H₂O as a function of the bias voltage. It clearly shows a fast increase around ±150 meV (±170 mV), which coincides with the bending mode of D₂O (H₂O). Therefore, the diffusion of Na⁺ hydrates must have been induced by the vibrational excitation in the one-electron process (Fig. 2b, inset). The diffusion direction is almost random when using a CO tip. However, the Na⁺ hydrates tend to diffuse towards the Cl⁻ tip, owing to the electrostatic attraction between the Na⁺ and the Cl⁻ at the tip apex (see Supplementary Fig. 6 for experimental evidence and theoretical support). This provides a convenient way to study the diffusion of hydrates.

¹International Center for Quantum Materials, School of Physics, Peking University, Beijing, China. ²Institute of Theoretical and Computational Chemistry, College of Chemistry and Molecular Engineering, Peking University, Beijing, China. ³Institute of Physics, Czech Academy of Sciences, Prague, Czech Republic. ⁴Department of Physics and Astronomy, London Centre for Nanotechnology, Thomas Young Centre, University College London, London, UK. ⁵State Key Laboratory for Mesoscopic Physics and School of Physics, Peking University, Beijing, China. ⁶Collaborative Innovation Center of Quantum Matter, Beijing, China. ⁷Regional Centre of Advanced Technologies and Materials, Palacky University, Olomouc, Czech Republic. ⁸CAS Center for Excellence in Topological Quantum Computation, University of Chinese Academy of Sciences, Beijing, China. ⁹Present address: Institute of Experimental and Applied Physics, University of Regensburg, Regensburg, Germany. ¹⁰These authors contributed equally: Jinbo Peng, Duanyun Cao, Zhili He. *e-mail: limei.xu@pku.edu.cn; gaoyq@pku.edu.cn; egwang@pku.edu.cn; yjiang@pku.edu.cn

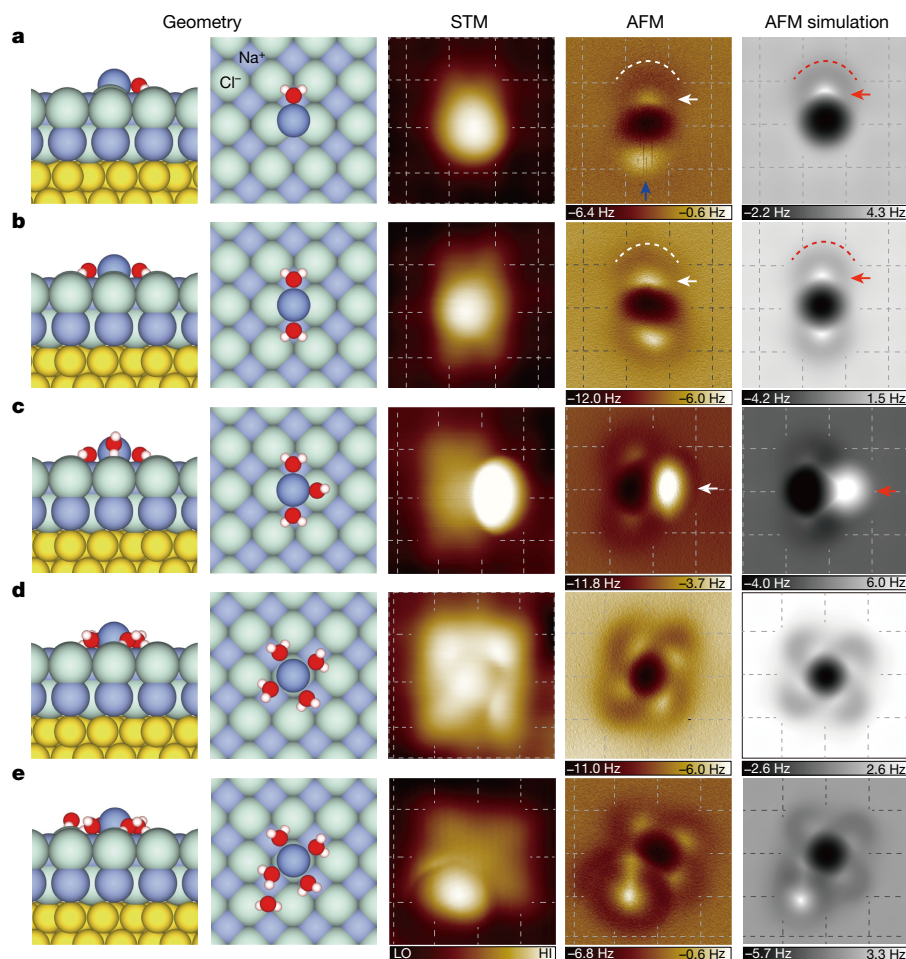


Fig. 1 | Geometries and high-resolution STM/AFM images of Na^+ hydrates. **a–e**, The atomic models (the first column shows the side view; the second column shows the top view), STM and AFM images (acquired with a CO tip) and AFM simulations of $\text{Na}^+ \cdot n\text{D}_2\text{O}$ clusters ($n = 1–5$), respectively. H, O, Cl, Na and Au atoms are denoted as white, red, green, purple and yellow spheres, respectively. Square lattices of the NaCl(001) surface arising from the Cl^- are depicted in the STM/AFM/simulation images by dashed grids. The white (red) arrows in **a** and **b** denote bright protrusions, and the white (red) dashed curves highlight the crooked depressions in the AFM images (AFM simulations). The blue arrow in **a** denotes the fuzzy feature arising from the flipping of the water molecule. The white (red) arrow in **c** denotes the standing water in the AFM image (AFM simulation). The set points of the STM images (**a–e**)

and $I = 20$ pA; $V = 150$ mV and $I = 30$ pA; $V = 100$ mV and $I = 30$ pA; $V = 100$ mV and $I = 50$ pA; and $V = 100$ mV and $I = 15$ pA, respectively. The tip heights of experimental (simulated) AFM images (**a–e**) are 130 pm (7.90 Å), 80 pm (8.10 Å), 100 pm (7.95 Å), 100 pm (8.10 Å) and 100 pm (7.99 Å), respectively. The tip height of experimental AFM images is referenced to the STM set point on the NaCl surface (100 mV, 50 pA). The tip height in simulations is defined as the vertical distance between the apex atom of the metal tip and the Na^+ ion in Na^+ hydrates. All the AFM oscillation amplitudes of experimental and simulated images are 100 pm. All the AFM simulations were done with a quadrupole (d_2) tip ($k = 0.75 \text{ N m}^{-1}$, $Q = -0.2e$, where Q is the magnitude of quadrupole charge at the tip apex and e is the elementary charge). The images are $1.5 \text{ nm} \times 1.5 \text{ nm}$.

To compare the mobility of different Na^+ hydrates, we adopted the following procedures: first, the Cl^- tip was positioned away from the hydrates at a certain lateral distance ($d \times$ the lattice constant of NaCl(001), which is 0.39 nm); second, the bias voltage was ramped slowly while the tip height was kept constant; and third, the tunnelling current experienced a sudden increase at a certain effective bias voltage (V_{eff}), signalling that the hydrates had reached the tip (Fig. 2c). We found that the as-determined V_{eff} increases as d increases (Fig. 2d). The behaviour of V_{eff} shows a negligible difference between the positive and negative biases, again revealing the critical role of the vibrational excitation (Fig. 2d).

Although the V_{eff} does not simply represent the diffusion barrier and is subject to various experimental parameters (Supplementary Fig. 7), we can still use this quantity to compare the relative mobility of different hydrates in a qualitative way. Figure 2e plots the V_{eff} as a function of d for different hydrates. We notice that $\text{Na}^+ \cdot 3\text{D}_2\text{O}$ has a much smaller V_{eff} than other hydrates. The hydrates never reached the tip for $d > 2$ even when the bias increased to 700 meV, except for $\text{Na}^+ \cdot 3\text{D}_2\text{O}$. We found that the tip may induce large structural change for $\text{Na}^+ \cdot 4\text{D}_2\text{O}$ and $\text{Na}^+ \cdot 5\text{D}_2\text{O}$ at

$d = 2$ (Supplementary Fig. 8), leading to a considerable reduction of V_{eff} . Strikingly, the $\text{Na}^+ \cdot 3\text{D}_2\text{O}$ can still diffuse to the tip readily at $d = 7$, with a relatively small V_{eff} (about 400 mV) (Fig. 2d). This suggests that the $\text{Na}^+ \cdot 3\text{D}_2\text{O}$ may have an unusually small diffusion barrier.

To gain insights into the diffusion pathway of those hydrates, we performed ab initio density functional theory (DFT) calculations (Methods). Indeed, the $\text{Na}^+ \cdot 3\text{H}_2\text{O}$ has the lowest diffusion barrier (below 80 meV) and the potential energy landscape along the path from the Cl^- bridge to Cl^- atop is rather flat, while all the other hydrates have barriers well above 200 meV (Fig. 3a). The initial, transition and final states are depicted in Fig. 3b. The diffusion of $\text{Na}^+ \cdot n\text{H}_2\text{O}$ ($n = 1–3$) is accompanied with the rotation of water around the Na^+ , whereas $\text{Na}^+ \cdot n\text{H}_2\text{O}$ ($n = 4$ and 5) follows a translational mode only with local rearrangements of water. The translational diffusion barrier of $\text{Na}^+ \cdot 3\text{H}_2\text{O}$ is almost three times that of the rotational one, while for $\text{Na}^+ \cdot 2\text{H}_2\text{O}$ and $\text{Na}^+ \cdot \text{H}_2\text{O}$ the barriers of the two modes are nearly the same (Supplementary Fig. 9).

The small diffusion barrier of $\text{Na}^+ \cdot 3\text{H}_2\text{O}$ is closely related to the existence of a peculiar metastable state (T3 in Fig. 3b), where the Na^+

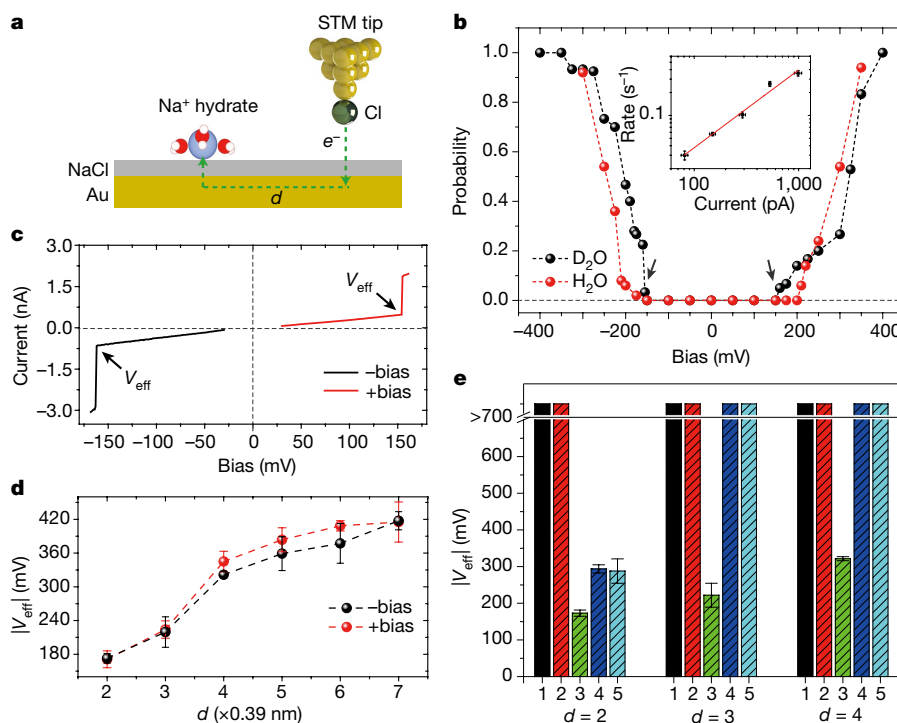


Fig. 2 | Tip-induced diffusion dynamics of Na⁺ hydrates. **a**, Schematic diagram of the Au-mediated inelastic electron excitation of the Na⁺ hydrates with the STM tip at a lateral distance of $d \times$ the lattice constant of NaCl(001), which is 0.39 nm. The flow direction of hot electrons is indicated by the green dotted arrow. **b**, Bias dependence of the diffusion probability of Na⁺·3D₂O and Na⁺·3H₂O with a CO tip at $d = 4$. The voltage pulse duration for each event is 1.2 s. The diffusion probability is a statistics from 50 events. The threshold bias for D₂O is indicated by two black arrows. The inset shows the current dependence of the diffusion rate of Na⁺·3D₂O with a CO tip at $d = 2$ under 170 mV. Error bars of

the current reflect the standard deviation from the set point. Error bars of the diffusion rate reflect the errors of exponential fitting of lifetime distribution. The solid line is the least-squares fit to the data with a power law, $R \propto I^N$, where $N = 1.02 \pm 0.08$, indicating a one-electron process. **c**, Current–bias relationship of Na⁺·3D₂O with a Cl[−] tip at $d = 2$, where the current jumps occur at V_{eff} . **d**, Lateral distance dependence of the positive (red) and negative (black) V_{eff} for Na⁺·3D₂O with a Cl[−] tip. **e**, Comparison of V_{eff} for Na⁺· n D₂O ($n = 1–5$) at $d = 2, 3$ and 4. Error bars in **d** and **e** reflect the standard deviation (up to 8 different datasets). The tip height in **b–e** is -165 pm referenced to the STM set point on NaCl (100 mV, 10 pA).

is located at the top Cl[−] site of NaCl, in contrast to the bridge site in the initial state. The conversion barrier between the initial and metastable states is only about 50 meV. The three H₂O molecules of Na⁺·3H₂O cannot simultaneously satisfy an optimal adsorption configuration either at the bridge site or at the top Cl[−] site owing to the symmetry mismatch with the tetragonal NaCl(001) surface. However, the structure of Na⁺· n H₂O ($n = 1, 2, 4, 5$) matches well with NaCl(001), stabilizing the hydrates at particular sites (bridge or top sites).

Furthermore, we found that the diffusion of Na⁺·3H₂O is coupled with a collective rotation of water in the metastable state (T6 to T11 in Supplementary Fig. 10). Such a rotation requires the water to make only slight adjustments and break minimal bonds with NaCl, leading to a small barrier (about 80 meV). However, removing one H₂O molecule from Na⁺·3H₂O may greatly increase the travelling distance of water during the rotation, while adding one H₂O molecule may block the rotational degrees of freedom owing to the perfect symmetry match between Na⁺·4H₂O and NaCl(001). Therefore, it is the degree of symmetry match between the hydrates and the surface that makes the diffusion barrier sensitive to the number of the water molecules.

These STM/AFM experiments were performed only at low temperature (5 K) and the calculated diffusion barriers correspond to the ones at 0 K. To investigate the surface diffusion at finite temperatures, especially close to room temperature, we carried out classical molecular dynamics simulations (Methods). Figure 4a shows the x – y diffusion trajectories of Na⁺· n H₂O ($n = 1–5$) during a period of 200 ns at 300 K, showing an extraordinarily high mobility of Na⁺·3H₂O (also see Supplementary Videos 1–5). In the zoom-in image (Fig. 4b), two different hopping behaviours were observed. Na⁺·H₂O and Na⁺·2H₂O hop between the bridge sites (Supplementary Videos 6

and 7), while Na⁺·4H₂O and Na⁺·5H₂O hop between the top Cl[−] sites (Supplementary Videos 9 and 10). Interestingly, Na⁺·3H₂O exhibits a composite behaviour that contains both hopping patterns (Supplementary Video 8). The calculated diffusion mean-square displacements (MSD) at different temperatures are shown in Fig. 4c, revealing that the specific hydration-number effect persists even at room temperature. It is striking that the mobility of Na⁺·3H₂O is more than one order of magnitude larger than that of other clusters at 225 K. We also notice that the diffusion of Na⁺·3H₂O is much faster than that of Na⁺ in bulk solution³⁰.

Supplementary Fig. 11 and Fig. 4d plot the free-energy landscape of different Na⁺ hydrates (Methods). The free-energy minima for Na⁺· n H₂O ($n = 1, 2$) and Na⁺· n H₂O ($n = 4, 5$) are located at the bridge sites and the top Cl[−] sites, respectively (Supplementary Fig. 11a–d). By contrast, the free-energy surface of Na⁺·3H₂O shows local minima at the Cl[−] sites in addition to the global minima at the bridge sites (Fig. 4d); these local minima can greatly facilitate the diffusion by truncating the barrier (Supplementary Fig. 11i). From the density distributions of Na⁺ and H₂O of the most stable and metastable Na⁺·3H₂O (Fig. 4e and f), we can identify two characteristic triangular structures (see black dashed triangles and insets, and Supplementary Video 8), closely resembling the initial/final and transition (T3) states obtained by DFT (Fig. 3b). The triangular structures of metastable Na⁺·3H₂O are distributed in four equivalent configurations (see the grey dashed triangles in Fig. 4f), arising from the small rotational energy barrier (about 80 meV) of the three water molecules around the Na⁺, which is much lower than the translational barrier (about 220 meV) (see Supplementary Fig. 9).

More generally, the specific hydration-number effect observed in this work may also exist for other salt ions (Li⁺, K⁺, Cl[−], and so

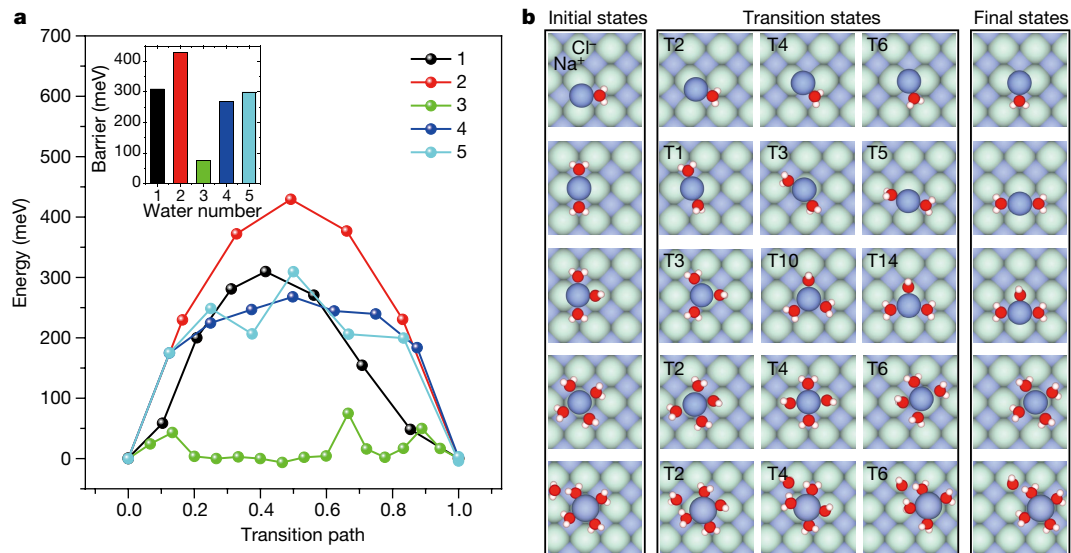


Fig. 3 | Calculated diffusion barrier of Na^+ hydrates by DFT.

a, Energy profiles for the diffusion of $\text{Na}^+ \cdot n\text{H}_2\text{O}$ ($n = 1-5$). The diffusion barriers are compared in the inset. **b**, Snapshots of Na^+ hydrates along the transition path. The first column, the middle three columns and the

last column represent the initial state, transition states and final state of $\text{Na}^+ \cdot n\text{H}_2\text{O}$ ($n = 1-5$), respectively. The number m in the T_m labels at the top left of the images corresponds to the $(m + 1)$ th data point in **a**.

on), but the hydration number can be different depending on the size and the hydration asymmetry of positive and negative ions (Supplementary Fig. 12). Therefore, our results point out a new way to control the ion transport in nanofluidic systems by interfacial

symmetry engineering^{6,9,10}. The techniques developed in this work can easily be extended to different ions and other hydration systems, opening up the possibility of studying various hydration processes down to atomic scale.

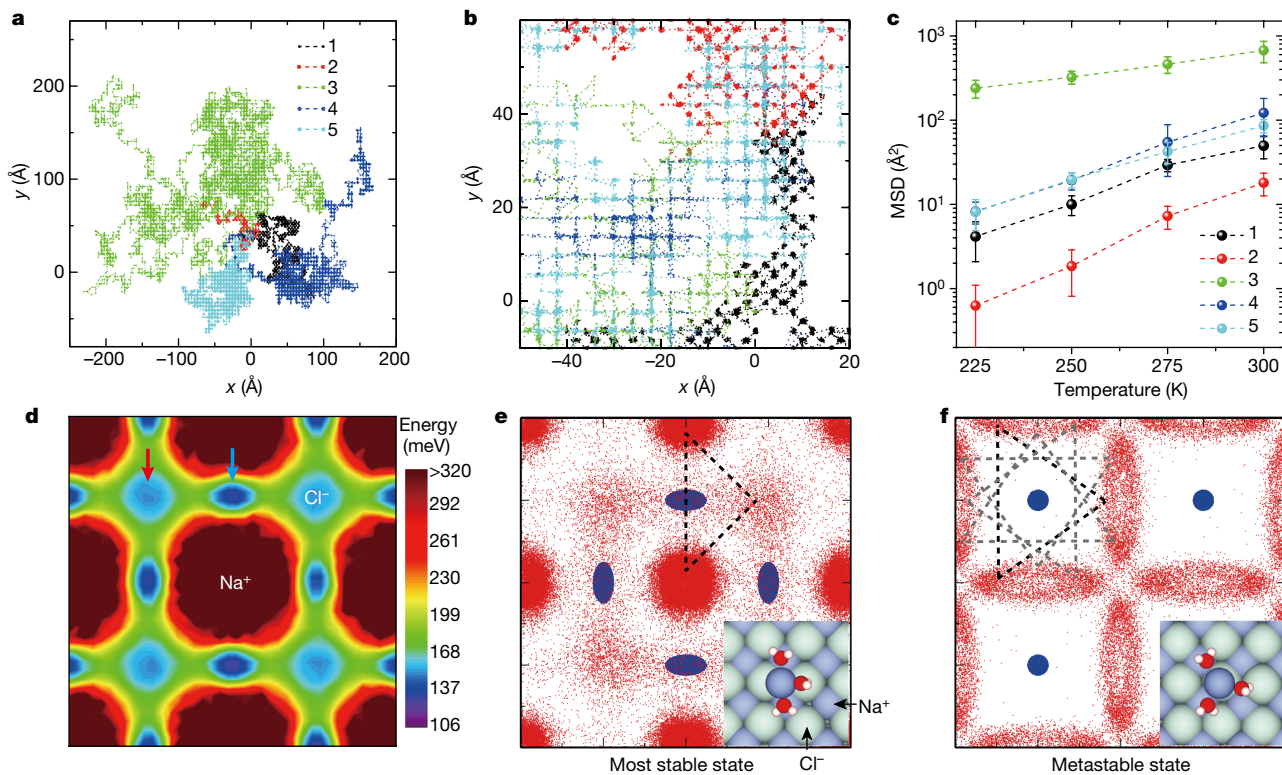


Fig. 4 | Molecular dynamics simulations of the diffusion of Na^+ hydrates at high temperatures. **a**, x - y trajectories of $\text{Na}^+ \cdot n\text{H}_2\text{O}$ ($n = 1-5$) during a period of 200 ns at 300 K. **b**, Zoom-in image of **a** showing different diffusion behaviours. The positions of Na^+ in two consecutive steps are connected by dotted lines. **c**, MSD in 1 ns of $\text{Na}^+ \cdot n\text{H}_2\text{O}$ ($n = 1-5$) between 225 K and 300 K. Error bars reflect the standard deviation from ten different datasets. **d**, The free-energy landscape experienced by $\text{Na}^+ \cdot 3\text{H}_2\text{O}$. It shows global minima at bridge sites (blue arrow) and local minima at top Cl^- sites (red arrow). The positions of Na^+ and Cl^- of the underlying $\text{NaCl}(001)$ surface are labelled. **e**, **f**, Density distributions of

the most stable and metastable $\text{Na}^+ \cdot 3\text{H}_2\text{O}$ on the same area of $\text{NaCl}(001)$ as **d** at 300 K. The blue and red dots represent the positions of Na^+ in the hydrate and of the O atom in H_2O , respectively. The position of Na^+ is constrained within an elliptical area centred at the bridge site (semi-major axis 0.5 Å and semi-minor axis 0.25 Å, **e**) and a circular area centred at the top Cl^- site (radius 0.25 Å, **f**). For clarity, the three water molecules within a representative $\text{Na}^+ \cdot 3\text{H}_2\text{O}$ molecule are connected with black dashed or grey lines. Insets of **e** and **f** are snapshots of $\text{Na}^+ \cdot 3\text{H}_2\text{O}$ at the bridge and top Cl^- sites, respectively. The images in **d-f** are 0.8 nm \times 0.8 nm; the insets in **e** and **f** are 1.2 nm \times 1.2 nm.

Online content

Any Methods, including any statements of data availability and Nature Research reporting summaries, along with any additional references and Source Data files, are available in the online version of the paper at <https://doi.org/10.1038/s41586-018-0122-2>.

Received: 18 September 2017; Accepted: 5 March 2018;

Published online: 14 May 2018

- Sipilä, M. et al. Molecular-scale evidence of aerosol particle formation via sequential addition of HIO_3 . *Nature* **537**, 532–534 (2016).
- Klimeš, J., Bowler, D. R. & Michaelides, A. Understanding the role of ions and water molecules in the NaCl dissolution process. *J. Chem. Phys.* **139**, 234702 (2013).
- Cohen-Tanugi, D. & Grossman, J. C. Water desalination across nanoporous graphene. *Nano Lett.* **12**, 3602–3608 (2012).
- Payandeh, J., Scheuer, T., Zheng, N. & Catterall, W. A. The crystal structure of a voltage-gated sodium channel. *Nature* **475**, 353–358 (2011).
- Gouaux, E. & MacKinnon, R. Principles of selective ion transport in channels and pumps. *Science* **310**, 1461–1465 (2005).
- Schoch, R. B., Han, J. & Renaud, P. Transport phenomena in nanofluidics. *Rev. Mod. Phys.* **80**, 839–883 (2008).
- Guo, W., Tian, Y. & Jiang, L. Asymmetric ion transport through ion-channel-mimetic solid-state nanopores. *Acc. Chem. Res.* **46**, 2834–2846 (2013).
- Whitby, M. & Quirke, N. Fluid flow in carbon nanotubes and nanopipes. *Nat. Nanotechnol.* **2**, 87–94 (2007).
- Stein, D., Kruithof, M. & Dekker, C. Surface-charge-governed ion transport in nanofluidic channels. *Phys. Rev. Lett.* **93**, 035901 (2004).
- Duan, C. & Majumdar, A. Anomalous ion transport in 2-nm hydrophilic nanochannels. *Nat. Nanotechnol.* **5**, 848–852 (2010).
- Omta, A. W., Kropman, M. F., Woutersen, S. & Bakker, H. J. Negligible effect of ions on the hydrogen-bond structure in liquid water. *Science* **301**, 347–349 (2003).
- Heisler, I. A. & Meech, S. R. Low-frequency modes of aqueous alkali halide solutions: glimpsing the hydrogen bonding vibration. *Science* **327**, 857–860 (2010).
- Tielrooij, K. J., Garcia-Araez, N., Bonn, M. & Bakker, H. J. Cooperativity in ion hydration. *Science* **328**, 1006–1009 (2010).
- Carrillo-Tripp, M., Saint-Martin, H. & Ortega-Blake, I. A comparative study of the hydration of Na^+ and K^+ with refined polarizable model potentials. *J. Chem. Phys.* **118**, 7062 (2003).
- Jungwirth, P. & Tobias, D. J. Specific ion effects at the air/water interface. *Chem. Rev.* **106**, 1259–1281 (2006).
- Kumagai, T. et al. H-atom relay reactions in real space. *Nat. Mater.* **11**, 167–172 (2012).
- Carrasco, J., Hodgson, A. & Michaelides, A. A molecular perspective of water at metal interfaces. *Nat. Mater.* **11**, 667–674 (2012).
- Guo, J. et al. Real-space imaging of interfacial water with submolecular resolution. *Nat. Mater.* **13**, 184–189 (2014).
- Maier, S. & Salmeron, M. How does water wet a surface? *Acc. Chem. Res.* **48**, 2783–2790 (2015).
- Shiotari, A. & Sugimoto, Y. Ultrahigh-resolution imaging of water networks by atomic force microscopy. *Nat. Commun.* **8**, 14313 (2017).
- Peng, J. et al. Weakly perturbative imaging of interfacial water with submolecular resolution by atomic force microscopy. *Nat. Commun.* **9**, 122 (2018).
- Meng, X. et al. Direct visualization of concerted proton tunnelling in a water nanocluster. *Nat. Phys.* **11**, 235–239 (2015).
- Fukuma, T., Ueda, Y., Yoshioka, S. & Asakawa, H. Atomic-scale distribution of water molecules at the mica–water interface visualized by three-dimensional scanning force microscopy. *Phys. Rev. Lett.* **104**, 016101 (2010).
- Ricci, M., Spijker, P. & Voitchovsky, K. Water-induced correlation between single ions imaged at the solid–liquid interface. *Nat. Commun.* **5**, 4400 (2014).
- Giessibl, F. J. Advances in atomic force microscopy. *Rev. Mod. Phys.* **75**, 949–983 (2003).
- Peng, J. et al. Atomic-scale imaging of the dissolution of NaCl islands by water at low temperature. *J. Phys. Condens. Matter* **29**, 104001 (2017).
- Gross, L. et al. The chemical structure of a molecule resolved by atomic force microscopy. *Science* **325**, 1110–1114 (2009).
- Gawronski, H., Carrasco, J., Michaelides, A. & Morgenstern, K. Manipulation and control of hydrogen bond dynamics in adsorbed ice nanoclusters. *Phys. Rev. Lett.* **101**, 136102 (2008).
- Stipe, B. C., Rezaei, M. A. & Ho, W. Single-molecule vibrational spectroscopy and microscopy. *Science* **280**, 1732–1735 (1998).
- Fuentes-Azcatl, R. & Barbosa, M. C. Sodium chloride, NaCl/ε: new force field. *J. Phys. Chem. B* **120**, 2460–2470 (2016).

Acknowledgements This work was supported by the National Key R&D Program under grant numbers 2016YFA0300901, 2017YFA0205003, 2016YFA0300903 and 2015CB856801; the National Natural Science Foundation of China under grant numbers 11634001, 11525520, 21573006 and 11290162/A040106; and the Key Research Program of the Chinese Academy of Sciences under grant numbers XDPB08-1 and XDPB08-4. Y.J. acknowledges support by the National Science Fund for Distinguished Young Scholars (grant number 21725302) and the Cheung Kong Young Scholar Program. P.H. and P.J. acknowledge support from the Czech Academy of Sciences project number MSM100101705 and Premium Academiae and GACR project number 18-09914S. J.G. acknowledges support from the National Postdoctoral Program for Innovative Talents. J.P. acknowledges support from the Weng Hongwu Original Research Foundation under grant number WHW201502. We are grateful for the computational resources provided by the TianHe-1A, TianHe II supercomputer, and the High-performance Computing Platform of Peking University. This work is supported in part by Songshan Lake Laboratory for Material Sciences.

Reviewer information Nature thanks P. Asinari and the other anonymous reviewer(s) for their contribution to the peer review of this work.

Author contributions Y.J. and E.-G.W. designed and supervised the project. J.P. performed the STM/AFM measurements (with J.G. and R.M.). D.C., J.C., X.-Z.L. and L.-M.X. performed ab initio DFT calculations. Z.H., W.J.X. and Y.Q.G. carried out the classical molecular dynamics simulations. P.H. and P.J. carried out the theoretical simulations of the AFM images (in collaboration with D.C. and B.C.). J.P., D.C., Z.H., J.G., W.J.X., X.-Z.L., Y.Q.G., L.-M.X., E.-G.W. and Y.J. analysed the data. Y.J. wrote the manuscript with input from all other authors. The manuscript reflects the contributions of all authors.

Competing interests The authors declare no competing interests.

Additional information

Supplementary information. is available for this paper at <https://doi.org/10.1038/s41586-018-0122-2>.

Reprints and permissions information is available at <http://www.nature.com/reprints>.

Correspondence and requests for materials should be addressed to L.-M.X. or Y.Q.G. or E.-G.W. or Y.J.

Publisher's note: Springer Nature remains neutral with regard to jurisdictional claims in published maps and institutional affiliations.

METHODS

STM/AFM experiments. All the experiments were performed with a combined noncontact AFM/STM system (Createc, Germany) at 5 K using a qPlus sensor equipped with a tungsten (W) tip (spring constant $k_0 \approx 1,800 \text{ N m}^{-1}$, resonance frequency $f_0 = 23.7 \text{ kHz}$, and quality factor $Q \approx 80,000$). The NaCl(001) bilayer film was obtained by thermally evaporating NaCl crystals onto a clean Au(111) surface at room temperature. To reduce the instability of water molecules induced by the vibrational excitation of inelastic electrons, we used deuterated water (D_2O) instead of H_2O in the experiment. The ultrapure D_2O (Sigma Aldrich, hydrogen-depleted) was used and further purified under vacuum by several freeze-and-pump cycles to remove remaining impurities. The D_2O molecules were dosed in situ onto the sample surface at 5 K through a dosing tube. Bias voltage refers to the sample voltage with respect to the tip. All of the STM topographic images and the AFM frequency shift (Δf) images were obtained with the CO-terminated tips in constant-current and constant-height mode, respectively. The CO tip was obtained by positioning the tip over a CO molecule on the NaCl island at a set point of 100 mV and 20 pA, followed by increasing the bias voltage to 200 mV²¹. The controllable manipulation of water molecules was achieved with the Cl^- -terminated tip at the set point $V = 10 \text{ mV}$, $I = 150 \text{ pA}$. The Cl^- tip was prepared by scanning the NaCl surface in closer proximity (below $V = 5 \text{ mV}$ and $I = 2.5 \text{ nA}$) with a bare metal tip until the Cl atom hopped onto the tip apex²². The construction of the Na^+ hydrates was done with the Cl^- tips (for details see Supplementary Fig. 1).

DFT calculations. DFT calculations were performed using the Vienna ab initio simulation package (VASP)^{31,32}. Projector augmented wave pseudopotentials were used with a cut-off energy of 550 eV for the expansion of the electronic wave functions³³. Van der Waals corrections for dispersion forces were considered by using the optB86b-vdW functional^{34,35}. In our study, the system consisted of a bilayer NaCl(001) on top of Au(111) substrate modelled by a four-layer slab if not specifically mentioned. Similar to ref. 18, a (2×2) NaCl(001) unit cell on a slightly deformed $\begin{pmatrix} 3 & 1 \\ 1 & 3 \end{pmatrix}$ superstructure of the Au(111) substrate was constructed as the surface model. The lattice constant for NaCl(001) surface was set to be 3.9 Å which is the same as in the experiment, and the Au(111) substrate was with a residual strain of about 2%. Supercells of this surface model were used to make the error of water-image interaction negligible with Monkhorst-Pack k -point meshes of spacing denser than $2\pi \times 0.0064 \text{ \AA}^{-1}$. The thickness of the vacuum slab was larger than 16 Å and the dipole correction was applied along the surface normal direction^{36,37}. The Au substrate and the bottom layer of the NaCl were fixed in simulations. The Na in the hydrates was positively charged with the charge nearly identical to the Na^+ of the NaCl substrate, based on the Bader charge analysis³⁸. Similar to ref. 22, the Cl^- -terminated tip was modelled using a three-layer Au pyramid of a [111] cleaved face with a Cl atom attached at the end. Energy barriers and paths for the diffusion of the hydration clusters were determined using the cNEB method^{39,40}. The geometry optimizations and the cNEB calculations were performed with a force criterion of 0.01 eV \AA^{-1} and 0.02 eV \AA^{-1} , respectively. The binding energies (E_{bind}) were calculated by subtracting the total energy of the Na^+ hydrates on the NaCl(001)/Au(111) structure from the sum of the energies of the relaxed bare NaCl(001)/Au(111) substrate, the gas phase of Na and the corresponding isolated water molecules in the gas phase (see Supplementary Fig. 13):

$$E_{\text{bind}} = E[(\text{NaCl}(001)/\text{Au}(111))_{\text{relaxed}}] + n \times E[(\text{H}_2\text{O})_{\text{gas}}] + E[(\text{Na})_{\text{gas}}] - E[(\text{NaCl}(001)/\text{Au}(111) + \text{Na}^+ \cdot n\text{H}_2\text{O})_{\text{relaxed}}]$$

Simulations of AFM images. The Δf images were simulated with a molecular mechanics model including the electrostatic force, based on the methods described in refs 41,42. We used the following parameters of the flexible probe-particle tip model: the effective lateral stiffness $k = 0.75 \text{ N m}^{-1}$ and effective atomic radius $R_c = 1.661 \text{ \AA}$. We added a quadrupole-like charge distribution at the tip apex to simulate the CO tip^{21,43} for all the AFM simulations. Comparison between the AFM images and theoretical simulations reveals that the key to the ultrahigh-resolution imaging lies in probing the weak high-order electrostatic force between the quadrupole-like CO-terminated tip and the polar water molecules or ions at large tip-sample distances, in clear contrast to traditional high-resolution AFM imaging at close distances where Pauli repulsion dominates²⁷. This weak interaction allows the imaging and structural determination of the weakly bonded hydrates without inducing any disturbance. The input electrostatic potentials of the Na^+ hydrates on the NaCl(001), employed in AFM simulations, was obtained from DFT calculations. Parameters of Lennard-Jones pairwise potentials for all elements are listed in Supplementary Table 1.

Molecular dynamics simulations. All the molecular dynamics simulation results shown in the paper were obtained by using polarizable force field parameters³⁰ that are developed based on molecular dynamics in electronic continuum theory⁴⁴. The model allowed reproduction of a range of physical and chemical properties of sodium chloride, including the density and the surface tension of pure crystal

system, the viscosity, the dielectric constant, and also the diffusion coefficient in solution³⁰.

The polarizable force field we used is based on a pairwise additive potential that includes a Coulombic treatment of the electrostatic interactions and a Lennard-Jones representation of dispersion-attraction and core repulsion. In this formulation, the potential energy E_{ij} between any pair of non-bonded atoms (i and j) in a system composed of the ions and water molecules is usually expressed as the sum of the van der Waals interaction energy E_{vdW} and the Coulombic interaction energy $E_{\text{Coulombic}}$, namely

$$E_{ij} = 4\epsilon_{ij} \left[\left(\frac{\sigma_{ij}}{r_{ij}} \right)^{12} - \left(\frac{\sigma_{ij}}{r_{ij}} \right)^6 \right] + \lambda_i \lambda_j \frac{q_i q_j}{4\pi\epsilon_0 r_{ij}}$$

Here, r_{ij} is the distance between the two atoms; q_i and q_j are the point charges of the atoms; ϵ_0 is the permittivity of vacuum; λ_i and λ_j describe the Coulombic polarizable effect of atoms; σ_{ij} and ϵ_{ij} are the distance at which the interparticle potential is zero and the well depth of the Lennard-Jones potential, respectively. Lorentz-Berteloth combination rules⁴⁵ were used to describe the van der Waals interaction between two different kinds of atoms. Our force field parameters are shown in Supplementary Tables 2 and 3.

To test the effect of force field parameters on the simulated results, we also used a non-polarizable force field parameter, where the SPC/E model was used for water⁴⁶ and the ion parameters were taken from Joung and Cheatham⁴⁷. The results show a consistent conclusion with the polarizable force field.

All classical molecular dynamics simulations were performed using the AMBER14 suite of programs⁴⁸. A four-layer NaCl crystal (atom numbers of $18 \times 18 \times 4$) with a (001) surface was built to support the Na^+ hydrates. Each simulation system was first subjected to 5,000 steps of steepest descent energy minimization, followed by 5,000 steps of conjugate gradient optimization. Then, a 100-ps molecular dynamics simulation was performed to heat the system up to the target temperature, followed by a 10-ns-long normal molecular dynamics simulation to further relax the system. After the initial equilibration, we performed 200-ns calculations for each system with a time step of 2 fs. The temperature was controlled using Langevin dynamics with a collision frequency of 1.0 ps^{-1} . Simulation using Nose-Hoover thermostat yields the same results. The bottom layer of NaCl crystal was restrained by the $2,000 \text{ kcal (mol \AA}^2)^{-1}$ force constant, and all classical molecular dynamics simulations were carried out with periodic boundary conditions on the crystal plane. The SHAKE algorithm was used to constrain all bonds involving hydrogen atoms⁴⁹. A cut-off of 1.0 nm was used for van der Waals interactions. A long-range dispersion correction based on an analytical integral assuming an isotropic, uniform bulk particle distribution beyond the cut-off was added to the van der Waals energy and pressure⁴⁸.

Owing to the limitations of our computational ability and the inherently stochastic property of diffusion calculated for small numbers of atoms, it is very difficult to obtain accurate diffusion coefficients (D) for different hydrates. By contrast, bulk calculations sample the trajectories of many more molecules in a more homogeneous environment compared to the current calculations of a cluster on the crystal surface, and are thus faster in yielding converged D values. Instead, we simply used MSD for every nanosecond (up to 20 ns) to compare the mobility of different hydrates. We took the average of MSD from ten different sets of 20-ns data and the error bar reflects the standard deviation.

The equilibrium fractional population distribution of Na^+ hydrates at different sites follows a Boltzmann distribution. The equilibrium ratio of state i is

$$\frac{N_i}{N_{\text{total}}} = \frac{e^{-E_i/RT}}{\sum_{k=1}^{N_{\text{total}}} e^{-E_k/RT}}$$

where e is Euler's constant and E_i is the relative energy of the i th state to the minimum energy state. R is the molar ideal gas constant and T is the temperature. At room temperature, the configurations of hydrates were fully sampled. Thus we used the equilibrium ratio to calculate the free energy landscape of different states, which is

$$\Delta G = -RT \ln \frac{N_i}{N_{\text{total}}}$$

The water orientational time correlation functions $C_2(t)$ were calculated as $C_2(t) = \langle P_2[\mu_{\text{wat}}(0) \cdot \mu_{\text{wat}}(t)] \rangle$, where P_2 is the second-order Legendre polynomial, and $\mu_{\text{wat}}(t)$ is the direction vector of the water dipole at time t .

Data availability. The data that support the findings of this study are available from the corresponding author on reasonable request.

31. Kresse, G. & Hafner, J. Ab initio molecular dynamics for liquid metals. *Phys. Rev. B* **47**, 558–561 (1993).

32. Kresse, G. & Furthmüller, J. Efficient iterative schemes for ab initio total-energy calculations using a plane-wave basis set. *Phys. Rev. B* **54**, 11169–11186 (1996).
33. Kresse, G. & Joubert, D. From ultrasoft pseudopotentials to the projector augmented-wave method. *Phys. Rev. B* **59**, 1758–1775 (1999).
34. Klimeš, J., Bowler, D. R. & Michaelides, A. Chemical accuracy for the van der Waals density functional. *J. Phys. Condens. Matter* **22**, 022201 (2010).
35. Klimeš, J., Bowler, D. R. & Michaelides, A. Van der Waals density functionals applied to solids. *Phys. Rev. B* **83**, 195131 (2011).
36. Neugebauer, J. & Scheffler, M. Adsorbate-substrate and adsorbate-adsorbate interactions of Na and K adlayers on Al(111). *Phys. Rev. B* **46**, 16067–16080 (1992).
37. Makov, G. & Payne, M. C. Periodic boundary conditions in ab initio calculations. *Phys. Rev. B* **51**, 4014–4022 (1995).
38. Henkelman, G., Arnaldsson, A. & Jonsson, H. A fast and robust algorithm for Bader decomposition of charge density. *Comput. Mater. Sci.* **36**, 354–360 (2006).
39. Henkelman, G. & Jonsson, H. Improved tangent estimate in the nudged elastic band method for finding minimum energy paths and saddle points. *J. Chem. Phys.* **113**, 9978–9985 (2000).
40. Henkelman, G., Uberuaga, B. P. & Jonsson, H. A climbing image nudged elastic band method for finding saddle points and minimum energy paths. *J. Chem. Phys.* **113**, 9901–9904 (2000).
41. Hapala, P., Temirov, R., Tautz, F. S. & Jelinek, P. Origin of high-resolution IETS-STM images of organic molecules with functionalized tips. *Phys. Rev. Lett.* **113**, 226101 (2014).
42. Hapala, P. et al. Mechanism of high-resolution STM/AFM imaging with functionalized tips. *Phys. Rev. B* **90**, 085421 (2014).
43. Ellner, M. et al. The electric field of CO tips and its relevance for atomic force microscopy. *Nano Lett.* **16**, 1974–1980 (2016).
44. Leontyev, I. V. & Stuchebrukhov, A. A. Polarizable molecular interactions in condensed phase and their equivalent nonpolarizable models. *J. Chem. Phys.* **141**, 014103 (2014).
45. Hansen, J. P. & McDonald, I. R. *Theory of Simple Liquids* 3rd edn (Academic Press, 2006).
46. Berendsen, H. J. C., Grigera, J. R. & Straatsma, T. P. The missing term in effective pair potentials. *J. Phys. Chem.* **91**, 6269–6271 (1987).
47. Joung, I. S. & Cheatham, T. E. Molecular dynamics simulations of the dynamic and energetic properties of alkali and halide ions using water-model-specific ion parameters. *J. Phys. Chem. B* **113**, 13279–13290 (2009).
48. Case, D. A. et al. *AMBER version 14*. <http://ambermd.org> (University of California, San Francisco, 2014).
49. Ryckaert, J. P., Ciccotti, G. & Berendsen, H. J. C. Numerical integration of the Cartesian equations of motion of a system with constraints: molecular dynamics of *n*-alkanes. *J. Comput. Phys.* **23**, 327–341 (1977).